

Numerical modeling of transport and accumulation of DNA on electronically active biochips

Samuel K. Kassegne^a, Howard Reese^a, Dalibor Hodko^{a,*}, Joon M. Yang^a, Kamal Sarkar^a, Dan Smolko^a, Paul Swanson^a, Daniel E. Raymond^b, Michael J. Heller^c, Marc J. Madou^d

^a Nanogen Inc., 10398 Pacific Center Court, San Diego, CA 92121, USA

^b Genoptix, 3398 Carmel Mountain Road, San Diego, CA 92121, USA

^c Department of Bioengineering, University of California at San Diego, 9500 Gilman Drive, La Jolla, CA 92093-0412, USA

^d Department of Mechanical and Aerospace Engineering, University of California at Irvine, Room #S3231, 4200 Engineering Gateway Building, Irvine, CA 92697, USA

Received 30 December 2002; received in revised form 8 March 2003; accepted 13 March 2003

Abstract

Transport and accumulation of biomolecules, particularly DNA, in active electronic chips are investigated through numerical modeling and experimental verification. Various geometric and design configurations of electronically active DNA chips are considered. Further, we investigate the effect of electric field distribution on practical design of flow cells and chips. Particular attention is focused on the geometric effects on current and electric field distribution which are well captured by a finite element method-based model. We demonstrate that these geometric effects are observed only in buffers of very low conductivity. We also demonstrate that numerical models which do not include the charge transfer mechanism between electrodes and the buffer solution will fail to predict the reduction of these geometric effects with increased buffer conductivity.

The review of the technology is based on computer simulation using a finite element-based computational model and experimental results of electric field distribution, DNA transport and accumulation. Comparison of theoretical results for electrophoretic DNA accumulation with those obtained from experiments and a simple analytical model is presented.

© 2003 Elsevier Science B.V. All rights reserved.

Keywords: Electrophoresis; Active electronic chip; DNA transport; Hybridization; Finite element analysis; Micro-electrodes

1. Introduction

The completion of the physical mapping of the human genome [1] has brought a significant increase in interest in genomics research and development. However, while the completion of the gene sequencing may seem to suggest the end of the genome era and the beginning of the proteomics era, in fact only one significant part of the genome era has been completed. Beyond the sequencing effort lies the development and maturation of DNA molecular diagnostics and eventually gene therapy.

The potential for DNA molecular diagnostics to revolutionize the medical diagnostic market is well recognized by the many commercial companies now developing technologies and assays for diagnostic purposes. Despite this recognition, market development for molecular diagnostics has been slow partly due to economical factors as well as

technical challenges. Speed, accuracy, sensitivity and reproducibility have been the mantra of technical development of molecular diagnostic tools.

The variety of technologies being developed to overcome the technical challenges are quite clever and intriguing; but it is probably fair to say at this time that no single technology has been able to overcome all the technical hurdles with complete success. Of particular interest to us are electronically active DNA micro-arrays. These arrays have demonstrated very high accuracy and rapid transport [2–4]. There are three assay functions that these electronically active arrays fulfill: transportation and concentration of target DNA at an array site, hybridization and stringency. In this paper, we focus on the concentration of target DNA.

The majority of DNA micro-array technologies depend on diffusion of target DNA to the array sites [5–7]. Diffusion dependent transport scales with the square root of time and often takes several hours to achieve efficient hybridization of DNA molecules to capture probes or fluorescent probes to the DNA amplicons anchored at the detector surface. This

* Corresponding author. Tel.: +1-858-410-4718; fax: +1-858-410-4650.
E-mail address: dhodko@nanogen.com (D. Hodko).

is one of the main impeding factors in making the passive DNA sensing faster and more accurate within short period of time. Convection is sometimes used to speed the transport process, but still the assay times can be an hour or longer.

On the other hand, electronically active DNA micro-arrays utilize electrophoresis as the transport mechanism. Electrophoresis has the advantage that transport scales linearly with time and electric field. Consequently, typical transport times are two minutes or less. We have developed micro-electro-optical DNA sensors where transport of biomolecules is achieved through electrokinetic forces [2–4,8–11]. An electrode array covered with a permeation layer with embedded DNA capture probes is used to control the transport of biomolecules and achieve their accumulation and hybridization at the electrodes. The various electrode arrays illustrated in Fig. 1 enable both DC and AC electrokinetic manipulation of biomolecules and particles in the detector cell. The arrays consist of patterned metal electrodes on an insulating substrate and are contained in a plastic housing equipped with fluidic conduits to manipulate sample and other electrolytes. The electrical field applied affects charged analyte biomolecules and particles as well as the ions in the fluid sample.

Aside from a dependence on electric field strength, electrophoretic transport of target DNA is critically dependent on the composition of the transport buffer [8]. In electrophoresis, the total current supplied by the external circuit is carried solely by the charged ions in solution. The portion of current carried by each ionic species is dependent on its charge, mobility and concentration and is known as the transport number. Because it is desirable to maximize the transport number of the target DNA, transport buffers are typically low salt, zwitterionic buffers: 50 mM histidine has functioned well for this purpose [3,8].

In this paper, we discuss the effects of array geometry on the accumulation of DNA during electrophoresis. Accumulation is modeled using an analytical model and finite element analysis (FEA) and the results are compared with experimental data.

The numerical and analytical modeling of such an electrophoretic system has been of some interest to a growing number of researchers in the past few years. The work of Stelzle et al. [12] is among the first in the literature that used analytical modeling to predict electric field in biochips. They have looked at increasing the efficiency of accumula-

tion through “focusing electrodes” and discussed general design principles for the case of a cylindrical shaped flow cell that contains chips with focusing electrodes. Paces et al. [13] were among the first group of researchers to report results in DNA accumulation and hybridization based on numerical modeling. They studied electrokinetic transport of charged species in an electrolyte and reviewed electric potential, electric field distribution and species transport in a chip array that consists of 5×5 electrodes. Their model was based on a two-dimensional finite element formulation. Based on their continuum model, they reported geometric effects on electric field with peaks at the edge electrodes. Ozkan [14] has also used the finite element method to study electric field distribution in an electronic chip array. Her work concentrated on investigating the effects of charged species concentration, size, position, type of buffer solution and patterned electrode configuration on the electric field distribution and hence the electrokinetic transport of charged species.

In this work, we investigate various configurations of active DNA chips where experimental results are available for qualitative and quantitative verifications. The quantities of interest for our study are DNA transport, accumulation and electric field distribution. We investigate the effect of electric field distribution on practical design of flow cells and chips. Particular attention is focused on the geometric effects which are well captured by a finite element-based model.

We will further show experimentally that, with increased conductivity of the buffer, such geometric effects are minimized and eventually eliminated. We suggest that the decrease in these geometric effects is caused by the decrease in polarization resistance as solution conductivity is increased. This decrease in polarization resistance in turn results in an increase in current contribution due to polarization (i.e. Faradaic current) that is significant enough to screen the effects of current contribution from solution resistance. Numerical models that do not explicitly include the polarization resistance in their formulation will fail in predicting the decrease and elimination of these effects with increased buffer conductivity.

2. Electronic accumulation of DNA

In this paper, two generations of electronically active micro-arrays were modeled and experimentally tested. The

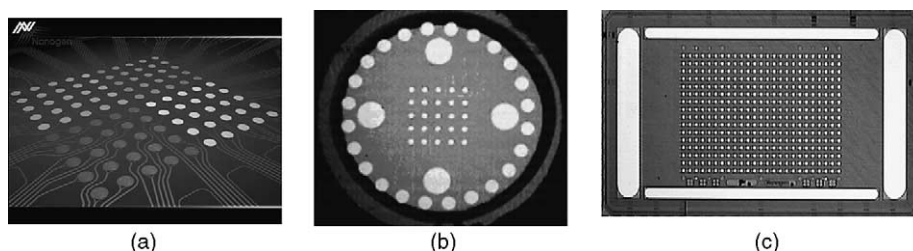


Fig. 1. Illustration of active DNA chips used in this study: (a) 100-site chip, NanoChip®; (b) 25-site chip, NanoChip®; (c) 400-site chip, NanoChip®.

early generation chips, shown in Fig. 1a and b are the 10×10 and 5×5 arrays of $80 \mu\text{m}$ diameter platinum electrodes spaced with $200 \mu\text{m}$ center-to-center distance. Four large counter-electrodes are located at the corners of the array. External circuitry was used to control the potential or current at the array electrodes, either one electrode at a time or in groups of electrodes. The chip was mounted in a probe station for electrical connection and fluorescent measurements. Liquid samples were manually applied to the chip.

The later generation chip, shown in Fig. 1c, is a 16×25 array of $50 \mu\text{m}$ diameter platinum electrodes spaced with $150 \mu\text{m}$ center-to-center distance. Two pairs of rectangular, individually controlled, counter-electrodes are aligned along the perimeter of the array. Not shown in Fig. 1a–c are off-chip Ag/AgO quasi-reference electrodes (QRE). The micro-array is flip-chip bonded to a ceramic substrate. The ceramic substrate is subsequently mounted in a plastic cartridge housing that contains a flow cell for liquid sample handling and an optical window for fluorescence measurements. An important feature of this latter generation chip is the presence of on-board circuitry that permits the current or potential of each electrode to be individually controlled and measured.

The micro-arrays shown in Fig. 1 are coated with a hydrogel. This coating is about $1 \mu\text{m}$ thick in dry state and up to $10 \mu\text{m}$ thick in wet state and serves two main functions. It provides attachment chemistry for anchoring DNA probes and it elevates the anchored probes above the electrodes. The coatings are made of agarose or acrylamide copolymers and contain covalently linked streptavidin to provide attachment sites for biotin labeled oligonucleotides.

During an assay, DNA capture probes, targets or amplicons are addressed to specific array electrodes. Typically, the array electrodes are biased at $+2.0 \text{ V}$ with respect to the Ag/AgO QRE. This causes electrophoretic migration of the DNA toward the biased electrodes. If the DNA probes are biotinylated, they will bind to streptavidin and be immobilized on the hydrogel coating.

In the numerical models that follow, which are based on the finite element method (FEM), we consider a simplified electrode system consisting of a single, central anode and cathode ring, both without a hydrogel coating. We will show that this simplified electrode system captures the essence of electrophoretic transport on micro-arrays. The model results show the electric field distribution and the accumulation of DNA at the anode. These results are compared with the experimental results.

The finite element analysis (FEA) is then extended to model the 16×25 micro-array. The main effort with this model is to demonstrate the effects of array geometry on the pattern of accumulation and electric fields.

2.1. Description of models and experiments

The computational model in this work is based on the finite element formulations for fluid flow, diffusion and elec-

trophoresis (i.e. movement of charged species relative to the carrier movement under the influence of electric field). Further, the finite element model of the electrokinetic flow problem is based on a combination of Poisson's equations, diffusion equation and Navier–Stoke's equations with appropriate electromigratory flux terms to represent the effect of applied electric field on carrier and/or charged species.

The Navier–Stoke's equations which are defined here to include the equations of mass conservation, momentum conservation, energy conservation and equation of state are given as

$$\frac{\delta\rho}{\delta t} + \nabla \cdot \rho v = 0 \quad (\text{mass conservation equation}) \quad (1)$$

$$\frac{\delta(\rho v)}{\delta t} + \nabla \cdot \rho v v = -\nabla P + \nabla \tau + \rho g + F \quad (\text{momentum equation}) \quad (2)$$

$$\frac{\delta e}{\delta t} + v \cdot \nabla e = \nabla \cdot (k \nabla T) + H + \Phi_e \quad (\text{energy equation}) \quad (3)$$

$$\rho = \text{constant} \quad \text{or} \quad \rho = \frac{P}{RT} \quad \text{or} \quad \rho = \rho(T) \quad (\text{equation of state}) \quad (4)$$

Now, for electrokinetic flow, the following equations hold true:

$$\nabla^2 \Phi = -\left(\frac{\rho_e}{\varepsilon}\right) \quad (5)$$

$$E = -\nabla \Phi \quad (\Phi \text{ is the electric potential}) \quad (6)$$

$$V_{ep} = \mu_{ep} E \quad (\text{electrophoretic mobility of the ion}) \quad (7)$$

The species transport equation is given as

$$\left(\frac{\delta c_i}{\delta t}\right) + V_{ep,i} \nabla c_i = D_i \nabla^2 c_i \quad (8)$$

where v is the local fluid velocity, ρ the density of the fluid, t the time, τ the shear (viscous) stress on fluid, g the acceleration due to gravity, F the body force, T the temperature, P the pressure, k the thermal conductivity of the fluid, H the source term, Φ_e the dissipation terms, e the internal energy of the system (given as $\rho C_p T$, where C_p is the specific heat of the fluid), E the electric field, Φ the electric potential, ρ_e the charge density, ε the permittivity, μ_{ep} the electrophoretic mobility of ion in its carrier species, V_{ep} the electrophoretic velocity of charged species, c the concentration of species, D the coefficient of diffusion and i is the species number.

Generally, the energy equation is coupled to the momentum and continuity equations through the variation of density with temperature and pressure as shown in Eq. (4). For incompressible flows, however, the variation of density is negligible and the Navier–Stoke's equations are decoupled.

The following assumptions are made in the finite element modeling of the electric field distribution and DNA accumulation in the active DNA micro-array:

1. The effect of the charges carried by the DNA species on the electric field is neglected.
2. The effect of permeation layer on the DNA transport and accumulation and electric field distribution is neglected.
3. The sample concentration is assumed to be small compared to the concentration of the buffer solution and the conductivity of the solution is considered to be uniform throughout the liquid volume.
4. Physical parameters such as diffusion coefficients, fluid viscosity, electrokinetic mobilities, and dielectric properties are considered constant.
5. Joule heating in the liquid volume is assumed to be insignificant and the temperature of the solution is considered to be uniform.
6. Charge transfer mechanism between electrodes and the buffer solution is not included in the model. This mechanism has a significance in reducing geometric effects.

2.1.1. Case of single-electrode system

Fig. 2 shows the chip geometry of a single-electrode system used in this study. It consists of a cylindrical flow cell having a depth of $500\ \mu\text{m}$ and a diameter of $1000\ \mu\text{m}$. The flow cell contains the buffer solution and recessed electrodes. The anode is of $80\ \mu\text{m}$ diameter and has a thickness of $100\ \text{nm}$ and is located at the center of the cylindrical flow cell. The cathode is placed at the outer rim of the cylindrical cell and has a width of $40\ \mu\text{m}$ and a thickness of $100\ \text{nm}$. This configuration closely mimics the electrode array chip configuration used in experiments.

2.1.1.1. FEA model of single-electrode system. Following are the parameters and constants used in the modeling. These values closely match the experimental conditions used in the modeling. The buffer solution is $50\ \text{mM}$ histidine with a conductivity of $60\ \mu\text{S}/\text{cm}$. A $5\ \text{nM}$ concentration of single strand 20-mer DNA (DNA₂₀) sample is used. The valency of the DNA sample is -20 and the DNA's electrophoretic mobility and diffusion constants are assumed to be $15,000\ \mu\text{m}^2/\text{V s}$ and $20\ \mu\text{m}^2/\text{s}$, respectively. A constant potential of $+2\ \text{V}$ is

applied at the anode and $-2\ \text{V}$ is applied at the cathode. This corresponds to a constant voltage mode of operation used in the experiments with the active DNA array.

Two modeling approaches are pursued in this study, i.e. a three-dimensional finite element analysis and a simplified analytical model. The finite element analysis (FEA) was carried out using the CoventorWare™ software from Coventor Inc. [15], while the simplified analytical model is based on a simple relationship between the current carried by DNA species and the total current in the chip, as described in Eqs. (10a)–(10c). The finite element simulation consisted of a finite element (FE) mesh for an axisymmetric slice of the flow cell ($500\ \mu\text{m}$ deep and $500\ \mu\text{m}$ wide) with 1395 eight-noded parabolic elements and a total number of 6108 nodes, as shown in Fig. 3. This mesh was selected after a convergence study on current density and electric field distribution. The FE mesh, as expected, is much more dense at the location of the electrodes due to the sharp corners in the geometry and also due to the high gradient of electric field and current density at these locations. At locations further from the electrodes, the mesh is noticeably coarser resulting in saving of computational time.

The following boundary conditions are used:

$$\frac{\delta\Phi}{\delta n} = 0 \quad (\text{at the side walls, i.e. side walls and the top wall are insulated}) \quad (9a)$$

$$\Phi = \text{constant} \quad (\text{at the anode and cathode}) \quad (9b)$$

$$J_i \cdot n = 0 \quad (\text{no species adhesion on side walls}) \quad (9c)$$

where J_i is the ionic flux of species “ i ”, $i = 1$, number of species types in the flow cell.

2.1.1.2. Analytical model for DNA transport. In the micro-arrays described above, the current carried by the DNA, J_{DNA} , is a fraction of the total current, J , carried by all the ionic species in solution [16]. This is expressed in Eq. (10a) where the conductivity of the solution due to the DNA, σ_{DNA} , is a fraction of the solution

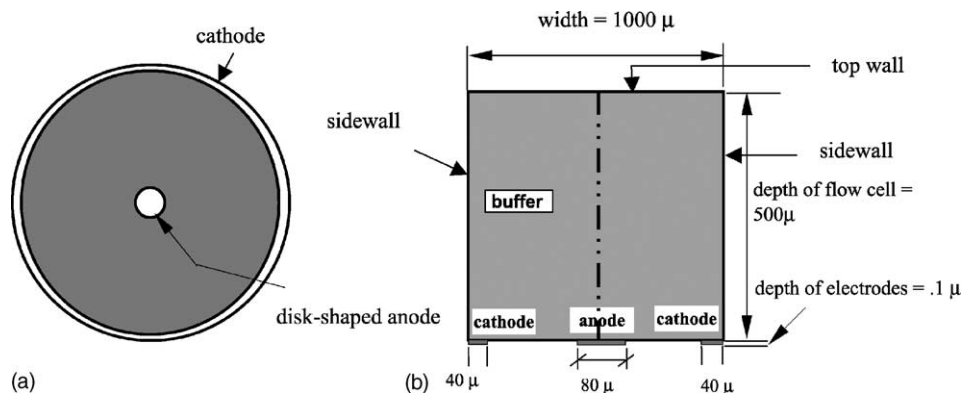


Fig. 2. Geometry of a ring single-electrode system in a cylindrical flow cell: (a) plan view of a ring electrode chip; (b) section view of the cylindrical flow cell.

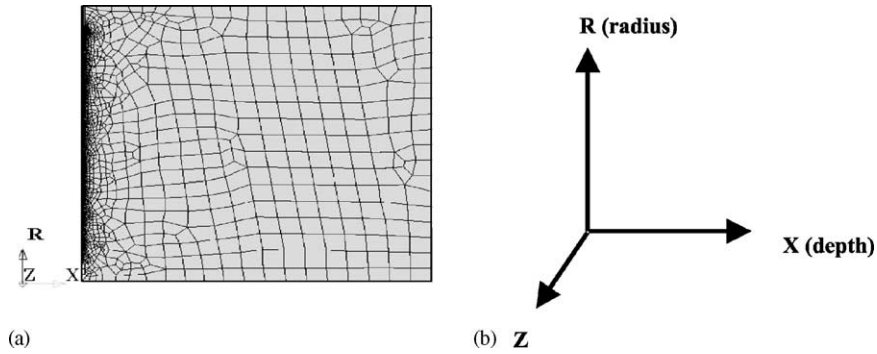


Fig. 3. Finite element mesh of an axisymmetric model of a cylindrical flow cell: (a) finite element mesh; (b) cylindrical coordinate system.

conductivity, σ :

$$J_{\text{DNA}} = \left(\frac{\sigma_{\text{DNA}}}{\sigma} \right) J \quad (10a)$$

By definition, the conductivity of the solution due to DNA is

$$\sigma_{\text{DNA}} = z c_{\text{DNA}} F \mu \quad (10b)$$

where z is the valence charge of DNA, c_{DNA} the concentration of DNA (in mol/l), F the Faraday's constant and μ is the mobility of DNA. Inserting Eq. (10b) into Eq. (10a) and rearranging we obtain

$$N_{\text{DNA}} = \left(\frac{F \mu}{e \sigma} \right) C_{\text{DNA}} J t \quad (10c)$$

where e is the electronic charge and N_{DNA} is the number of DNA molecules transported in a given time, t , for a given current, J . We define the number of DNA molecules accumulated at an array electrode divided by the total number of DNA molecules in the flow cell as the percent accumulation:

$$\text{accumulation (\%)} = \frac{N_{\text{DNA}}}{N_{\text{in flow cell}}} \times 100 \quad (10d)$$

where t is time (s).

The parameters used for the analytical model are $\mu = 15,000 \mu\text{m}^2/\text{V s}$, $\sigma = 60 \mu\text{S}/\text{cm}$, $c = 5 \text{ nM}$ and $J = 400 \text{ nA}$.

2.1.1.3. Experimental conditions for single-electrode system.

The sample used for the experimental DNA accumulation studies was a 5 nM solution of a fluorescently labeled T12 oligonucleotide in 50 mM histidine. An amount of 10 μl of this sample was placed on a 25-site micro-array (Fig. 1b) coated with an agarose/streptavidin permeation layer. One of the array sites was addressed at a constant current setting of 400 nA per pad for 60 s. The accumulation of fluorescence over the array site was monitored during the 60 s address and was measured with a Princeton Instrument CCD-based camera system using target DNA containing a Bodipy Texas Red (BTR) fluorescent tag. A 594 nm excitation filter and a 630 nm emission filter was used with the BTR labeled probe. The resulting fluorescence signal was quantified by comparison to fluorescent standards of known concentration.

2.1.2. Case of multi-electrode system

The second set of computer simulations was run on a 400 independently controlled electrode pad system shown in Fig. 1c. The electrodes are configured in a 16×25 rectangular distribution and have each a diameter of 50 μm with center-to-center spacing of 150 μm . There are two sets of counter-electrodes placed on the periphery of the chip system. These are a pair of long and short counter-electrodes which are always biased in pairs. The short counter-electrodes, which run in the transverse direction, are 500 μm wide and about 3300 μm long. The long counter-electrodes, which run in the longitudinal direction, are 190 μm wide and about 5500 μm long. The chip's overall dimension is 7.5 mm \times 4.5 mm with a depth of about 0.5 mm.

2.1.2.1. FEA model for multi-electrode system.

A two-dimensional model of the multi-electrode system is used in this study with the finite element mesh and coordinate system as shown in Fig. 4. Different sets of columns of electrodes were biased for the simulations. The finite element model for the case of column 1 electrodes biased has 8650 parabolic elements and 15,450 nodes. The voltage applied at the anodes is a constant voltage of 2 V, whereas a -2 V was applied at the counter-electrodes. In this study, the effect of permeation layer on electric field and accumulation was not modeled, as we were interested only in electric field and current distribution. To be consistent, the chips used in the experiments did not have permeation layer, either.

2.1.2.2. Experimental description for multi-electrode system.

The system was simulated to operate in *constant voltage* mode. This corresponds to a maximum current of 110 nA at the anodes. The chips used in the experiments did not have a permeation layer. The voltages at the electrodes and counter-electrodes were set through the software interface. Current readings on each of the electrodes were taken automatically by a software-controlled CMOS chip every quarter of a second. Different buffers were used in the experiments and for each reported result, the corresponding buffers and their concentration is given. The counter-electrodes were always biased in pairs.

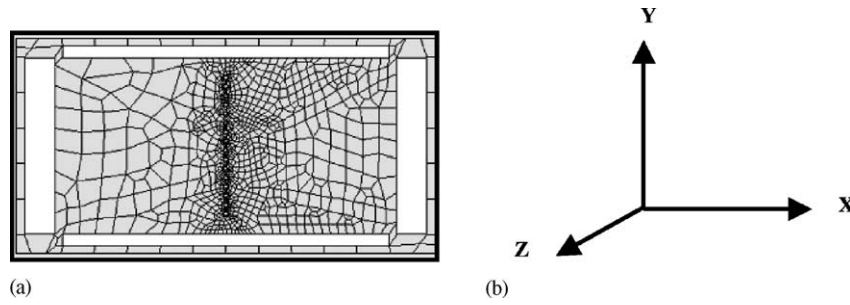


Fig. 4. Finite element mesh of a multi electrode array system with the center column of electrodes biased: (a) finite element mesh; (b) coordinate system.

3. Simulation results

This section presents some of the important numerical results obtained from the simulation of the electrochemical cells. The key quantities of interest covered in this study are, electric field distribution, transport and accumulation of DNA species.

3.1. Single-electrode system

Our numerical simulation indicates that, as soon as the electric field is applied, DNA starts moving towards the anode where it is accumulated. At the cathode, DNA is repelled due to its negative polarity. This onset of transport of DNA species in the flow cell of the active DNA micro-array depends primarily on the electric field distribution. There-

fore, a significant part of our modeling efforts was focused on looking at the qualitative and quantitative distribution of electric field in the flow cell. All simulation results shown in Figs. 5–7 apply to the axisymmetric section of the cylindrical flow cell.

In Fig. 5, it can be seen that the electric field distribution depicted by field vectors is most dense at the anode located in the center and to a lesser extent at the cathode located at the periphery. It is in these regions, therefore, where transport of DNA species is highest. Further, note that depth-wise (*x*-axis), the electric field is very sparse far from the electrodes suggesting that accumulation from these regions will be significantly slower. The radial distribution of the electric field, plotted in Fig. 5b, shows clear peaks at the anode and cathode (at the cathode, the peaks are much lower). Further, a closer look at Fig. 5b reveals that the electric

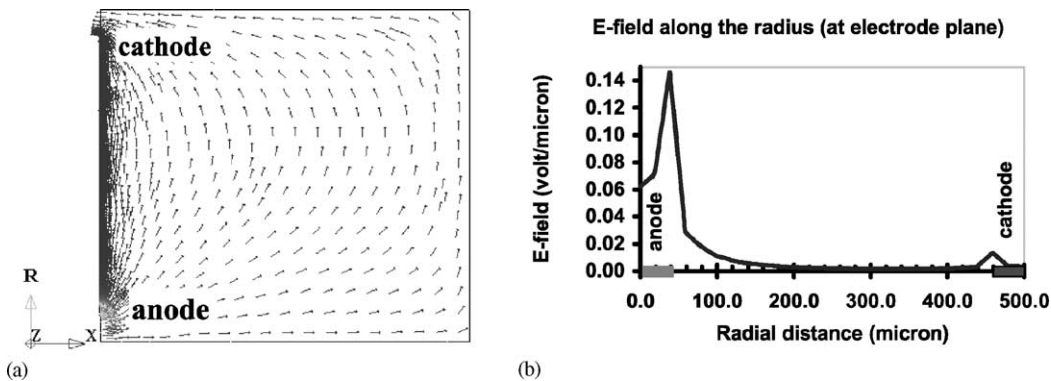


Fig. 5. Electric field distribution in the flow cell (units are in V/ μ m): (a) electric field vectors in axisymmetric model of flow cell; (b) electric field distribution along the radius of the chip. Anode is at origin.

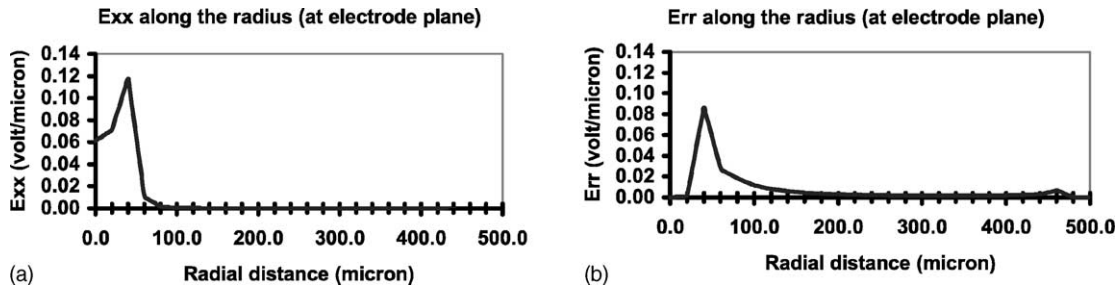


Fig. 6. Distribution of the vectorial components of electric field in the flow cell: (a) E_{xx} —the depth component of electric field; (b) E_{rr} —the radial component of electric field.

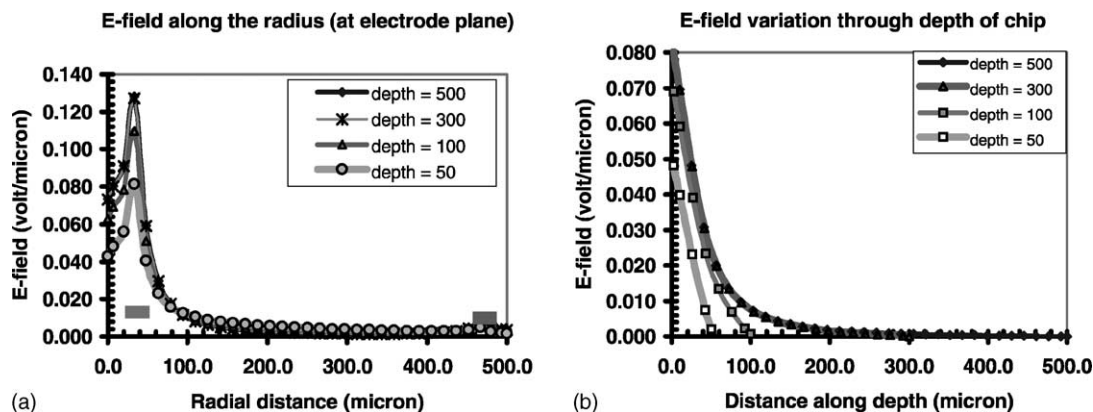


Fig. 7. Effect of depth of flow cell on electric field distribution: (a) electric field along the radius (depth in μm); (b) electric field along the depth of chip (depth in μm).

field is highest at the edge of the electrodes. Consequently, we expect greater accumulation of DNA at the periphery of the anode. This peak in electric field at the edges of the electrodes is consistent with previous analyses of disk electrodes that showed a higher current density at the periphery [17,18]. Moreover, at the edge of electrodes, the finite element mesh used should be as refined as possible to capture this significant peak at the edges. A significant amount of work in successfully modeling the edge effects in recessed micro-electrodes has been reported in the literature [18].

Fig. 6a and b show the depth (x) and radial (r) components of the electric field distribution for the axisymmetric model. The figures suggest that the depth-wise component of the electric field (i.e. E_{xx} in the axisymmetric model) is much higher than its radial component. We also investigated the effect of flow cell depth on electric field distribution by varying the depth of the cell for a given flow cell diameter and electrode spacing. The microfluidics module of IntelliSuite™ [19] was used for these simulations. The results are summarized in Fig. 7a and b which show that

the maximum electric field intensity at the edge of the anode drops only by one-third to one-half when the depth is reduced by 10-fold. The reduction of flow cell depth from 500 to 300 μm resulted in only about 15% drop of maximum electric field intensity. Moreover, away from the edge of the anode, the drop in electric field intensity is negligible. Fig. 7b shows the electric field distribution along the depth of the cell at the center of the flow cell. The figure shows that the electric field strength drops fast in the first 100 μm or so of depth. Therefore, from electric field strength and distribution point of view, the flow cell depth could be lowered to as much as 100 μm with little change in the magnitude of electric field strength and species accumulation rate. However, our experience with active DNA chips shows that considerations of allowing more volume for oxidation, bubble formation and oxygen saturation dictate that a higher flow cell depth of such as 500 μm be used. Fig. 8 shows the simulation results for the accumulation of DNA at the surface of the anode with respect to time. The DNA accumulation at the anodes was followed for 150 s at which time an onset

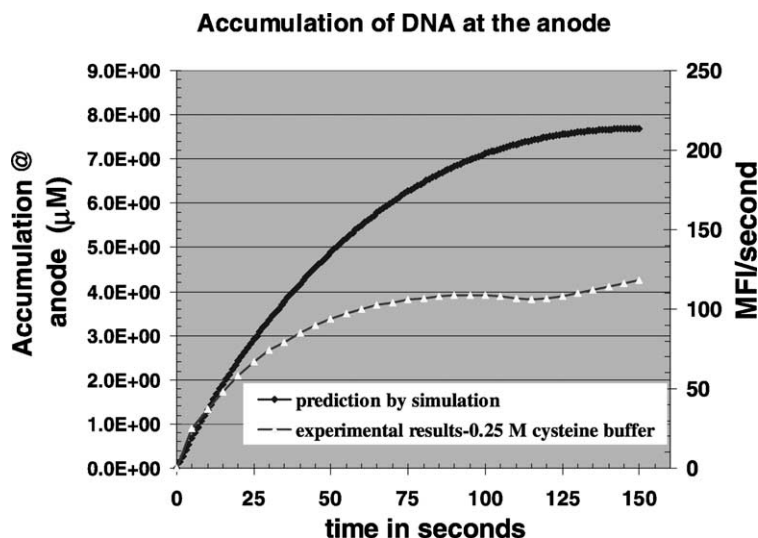


Fig. 8. Accumulation of DNA at the anode with respect to time.

Table 1
Comparison of DNA accumulation results from experiments and numerical models

	Percentage accumulation of DNA			
	10 s	30 s	60 s	90 s
Experimental result	<1	<1	1	–
Analytical model	<1	0.95	1.9	2.8
FEA model	<1	1.2	2.5	3.5

of saturation was observed. This result compares favorably with the experimental results also shown in Fig. 8.

Quantitative results for the percent accumulation are shown in Table 1. Here, the results for the FEA simulation, the analytical model and the experimental results are compared. While comparing results, it has to be noted that the theoretical models and the experimental observation have limitations. For example, the FEA simulation does not account for the buffering effect of the histidine transport buffer. Similarly, the analytical model does not account for diffusion of DNA as the concentration of DNA increases at the anode. The experimental accumulation results are based on an optical detection system that consists of a camera system that gave a focal depth of field of approximately 10 μm directly above the surface of the chip. The fluorescent data was, therefore, due to the accumulation of fluorescence only in the 10 μm deep column above the electrode. However, despite these limitations, we see that the model results and the experimental results agree reasonably well. Consequently, we believe that the analytical model and the FEA simulation capture the essence of DNA accumulation and

that other phenomena not accounted for in the models are of secondary importance. The FEA simulation discussed here, however, does not model the chemistry of the histidine buffer where such effects as the consumption of H^+ ions by histidine, and the generation of hydrogen and hydroxyl ions could introduce change in pH, which in turn will affect the analyte, and species transport properties in the flow cell.

The results from finite element analysis, experiment and analytical model confirm that indeed the electrophoretic accumulation of DNA occurs within few seconds and minutes, as compared to passive hybridization which sometimes could take hours. Table 1 also demonstrates that by increasing the accumulation time, significantly higher concentration of DNA is achieved at the anode. This result provides a basis for optimizing the DNA accumulation time with respect to the number of electrodes addressed and the targeted detection limits.

3.2. Results for multi-electrode system

In the following simulations of the 400-site chip (shown in Figs. 1c and 4), the conductivity of the solution is taken as 60 $\mu\text{S}/\text{cm}$, equivalent to that of a 50 mM histidine. The effects of the buffer conductivity are important and will be discussed later. The coordinate system used for the multi-electrode setup is given in Fig. 4b.

Fig. 9a shows the electric potential distribution on the 400-site chip when only the first column of array electrodes (total of 16 electrodes) and the short and long counter-electrodes were biased. It is clear that the potential peaks at the array electrodes and falls off rather quickly

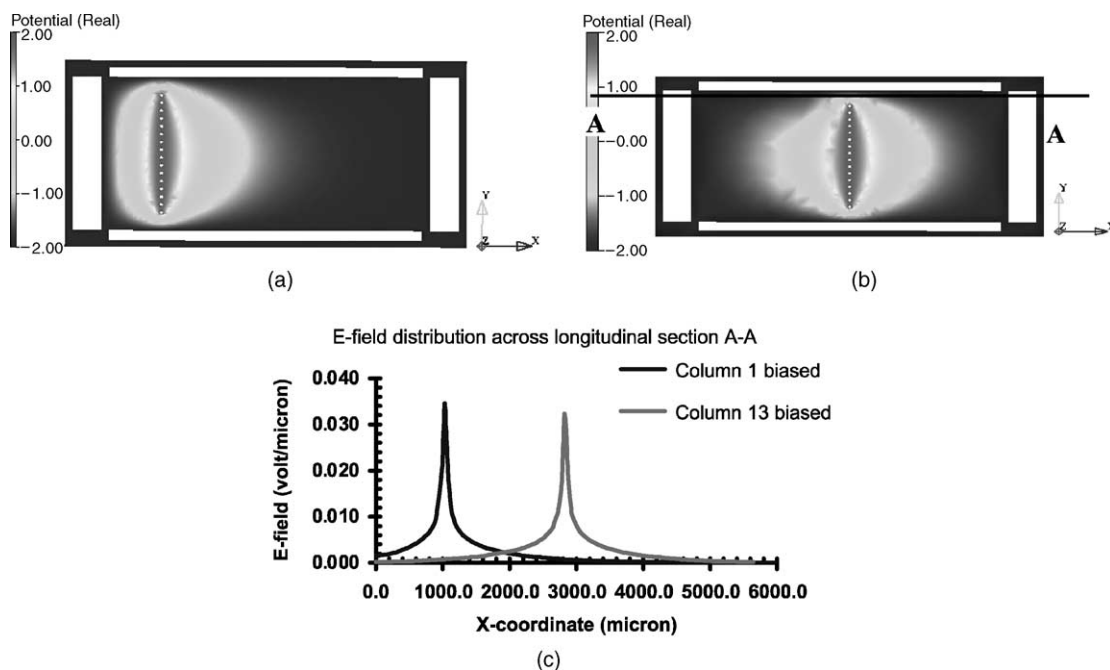


Fig. 9. Distribution of electrical potential and electric field in a 400-site chip with electrodes biased in a column-wise fashion: (a) electrodes on column 1 biased; (b) electrodes on column 13 biased (center of chip); (c) electric field distribution across longitudinal section A–A.

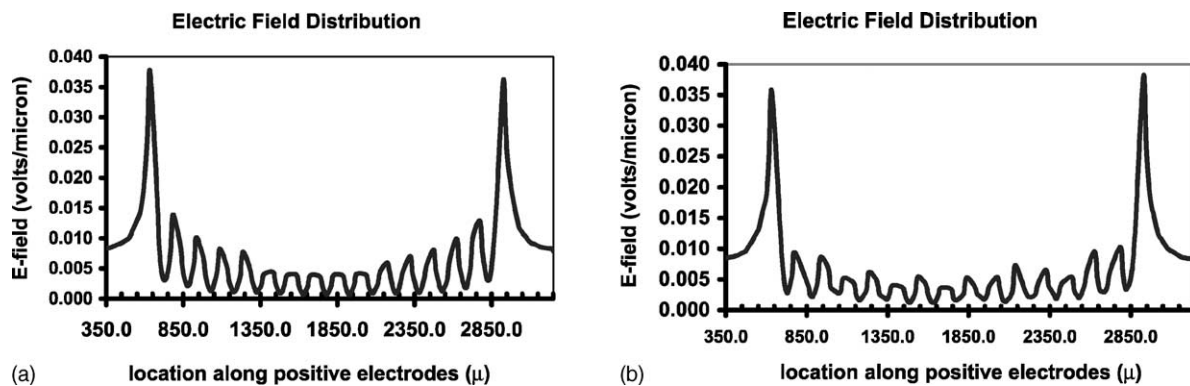


Fig. 10. Electric field distribution in a 400-site chip with electrodes at the first column biased: (a) distribution of electric field when column 1 biased; (b) distribution of electric field when column 13 biased.

with distance from the electrodes. In Fig. 9b where the center column of array electrodes is biased (column 13), the potential also drops off rather quickly with distance. The oval shape of the contour of potential in both cases is due to the effect of counter-electrodes that are placed at an angle to each other. Fig. 9c shows how the magnitude of the electric field intensity drops with distance when electrode arrays on columns 1 and 13 are biased. For example, when column 1 electrodes are biased, the electric field intensity drops by as much as 80% at a distance of only 200 μm away from centers of the biased electrodes. This distance roughly approximates the location of the center of the next set of electrode array. Fig. 10a and b show the electric field distribution corresponding to the biasing conditions illustrated in Fig. 9a and b, respectively. The field is observed to peak at the two outer array electrodes then drop quite dramatically for all of the inner array electrodes. This is mainly a geometric effect wherein the field between the inner array electrodes and the long counter-electrodes is screened by the outer array electrodes. More detailed discussion on this important observation is given in Section 3.4.1.

3.2.1. Effect of location of electrodes on current and electric field distributions

To determine the effect of location of the biased electrodes on the electric field distribution, subsequent simulations were run where interior columns of electric pads were biased. For this study, electrodes in columns 1, 13 and 25 were biased independently. As expected, there is always a peak in electric field in the outer electric pads. A comparison of Figs. 10a and b and 11a–d shows that as the column of biased array electrodes moves toward the center of the chip, the intensity of the field decreases on the two outer array electrodes and on the inner array electrodes. Again, this is due to the enhanced screening of the inner array electrodes by the two outer array electrodes.

3.2.2. Effect of counter-electrodes on current and electric field distribution

To determine the effect of the counter-electrodes on electric field distribution, two additional simulations were

run. The center column of array electrodes (column 13) was positively biased, but in one simulation only the long counter-electrodes were negatively biased, whereas in the other simulation only the short counter-electrodes were biased. The differences in the electric field distributions are shown in Fig. 13. When only the short counter-electrodes are biased, we see that the magnitude of the electric field is considerably reduced compared to the cases where only the long counter-electrodes are biased or where all the counter-electrodes are biased. We also notice that the difference in electric field strength between the two outer array electrodes and the inner array electrodes is less when only the short counter-electrodes are biased.

Once again, the geometry of biased electrodes plays an important role on the electric field strength at the various array electrodes. With only the short counter-electrodes being biased, the field lines between the array electrodes and the short counter-electrodes is approximately the same for all array electrodes. However, when only the long counter-electrodes are biased the two outer array electrodes screen the long counter-electrode from the inner array electrodes. In fact, the comparison in Fig. 12 shows that the distribution of field intensities is almost entirely due to the screening of the long counter-electrodes. Biasing rows of electrodes instead of columns essentially produces a qualitatively similar type of electric field and current distribution as that of biasing columns of electrodes.

3.3. Accumulation of DNA at anode

Computer simulations based on FEA models were also used to investigate accumulation of DNA on the anodes. Interesting results were obtained that may have a bearing on the design of biochips and, more importantly, assays. In this particular simulation, a bias of +2 and -2 V was used at the anode and cathode, respectively. Fig. 13 shows the moving front of DNA as it is transported on a symmetrical half of a 100-site chip (Fig. 1a) with the first column of array electrodes positively biased. The sides of the chip are assumed to be counter-electrodes. The effect of counter-diffusion that may be significant, as discussed before, is neglected here.

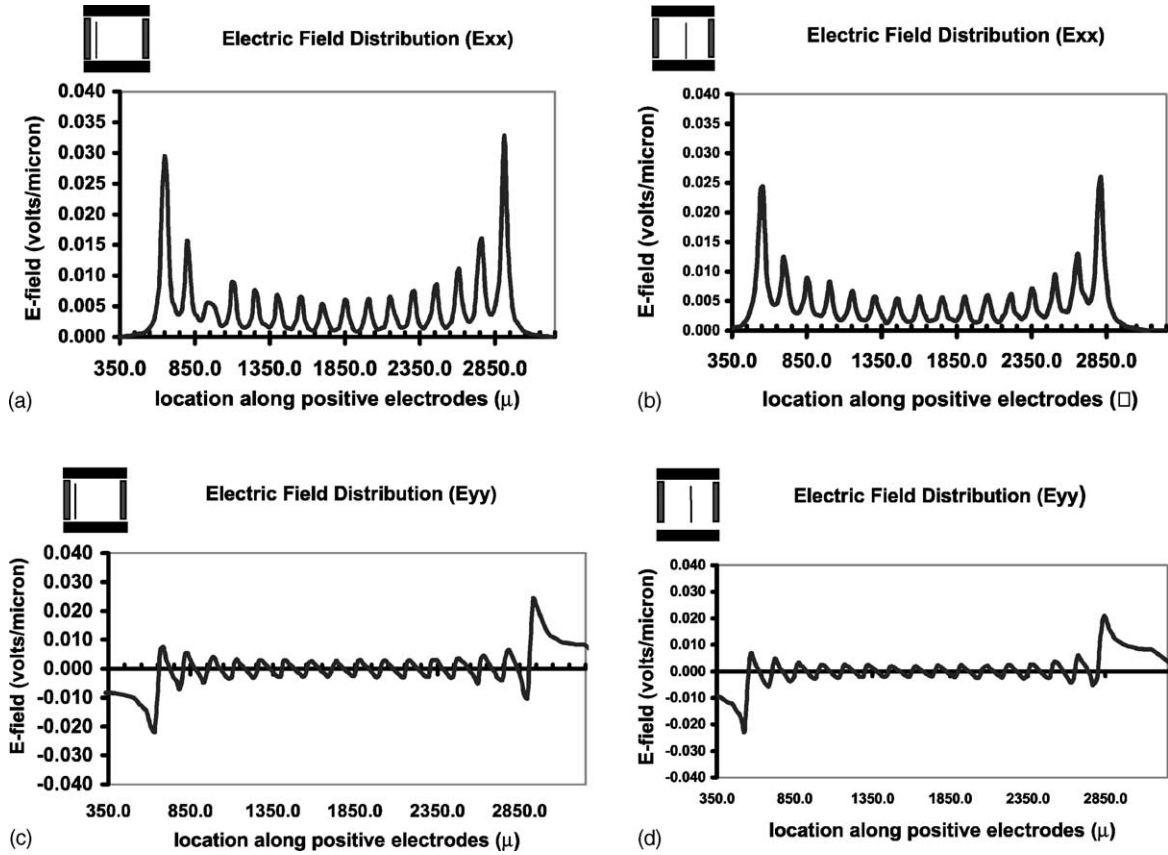


Fig. 11. Effect of location of biased electrodes on electric field distributions and intensity: (a) E_{xx} —the x -component of electric field at column 1; (b) E_{xx} —the x -component of electric field at column 13; (c) E_{yy} —the y -component of electric field at column 1; (d) E_{yy} —the y -component of electric field at column 13.

In the first few seconds, DNA nearest to the anodes is preferentially accumulated and leaves behind a depletion zone. Later, at $t = 40$ s, we notice that the area surrounding the upper array electrodes has become depleted of DNA and now only the lower array electrodes continue to accumulate DNA. The band of DNA movement that starts around the top

left corner then extends to the biased electrodes. DNA material at the top right corner is the last one to be transported to the column of anodes. Further, it needs to be noted that DNA is accumulated first at the biased anodes on the outer edges. The interior anodes will see accumulation of DNA species only slightly at the beginning. However, the DNA species

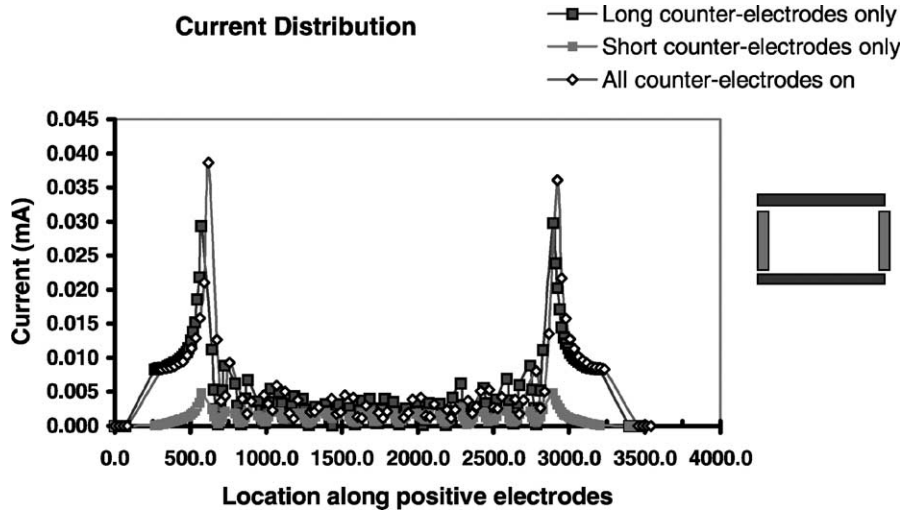


Fig. 12. Effect of counter-electrode configuration on electric field distributions and intensity.

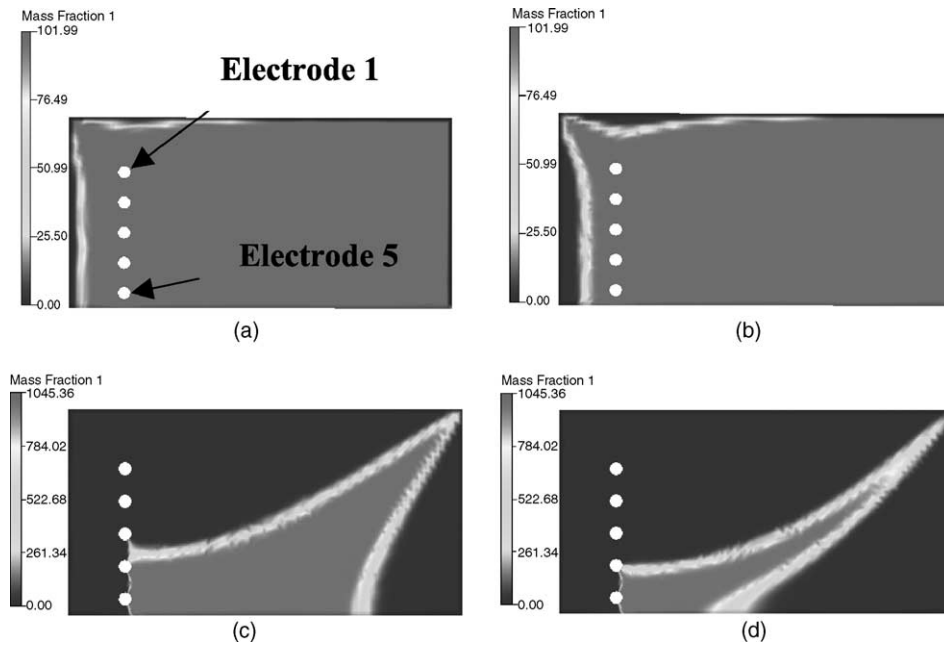


Fig. 13. Change in accumulation with time in a symmetrical half of a 100-site chip with biased electrodes at the first column: (a) $t = 3$ s; (b) $t = 5$ s; (c) $t = 40$ s; (d) $t = 90$ s.

in the bulk of the chip volume will accumulate at these interior pads as shown in Fig. 13. This is not unexpected, as DNA species travel along the streak lines shown in Fig. 15. The movement of DNA species shown in Fig. 14 closely follows these streak lines. The top left electrode on the chip has stronger electrical fields (cf. Fig. 10) but a smaller region that drains to it as shown by the streak lines that pass through it. On the other hand, the middle electrode shown in the bottom of the symmetrical-half of the chip has a relatively

weaker electric field strength; but a far larger volume of species draining to it. What happens is, therefore, that the top electrode will first see a fast but decreasing accumulation rate while the bottom electrodes will see a relatively slower albeit higher volume of accumulation (Fig. 14).

Fig. 14 shows the accumulation of DNA species over time at each of the five electrodes being investigated in this model. In the first few fractions of a second of biasing, the outer-edge electrode seems to accumulate the most amount

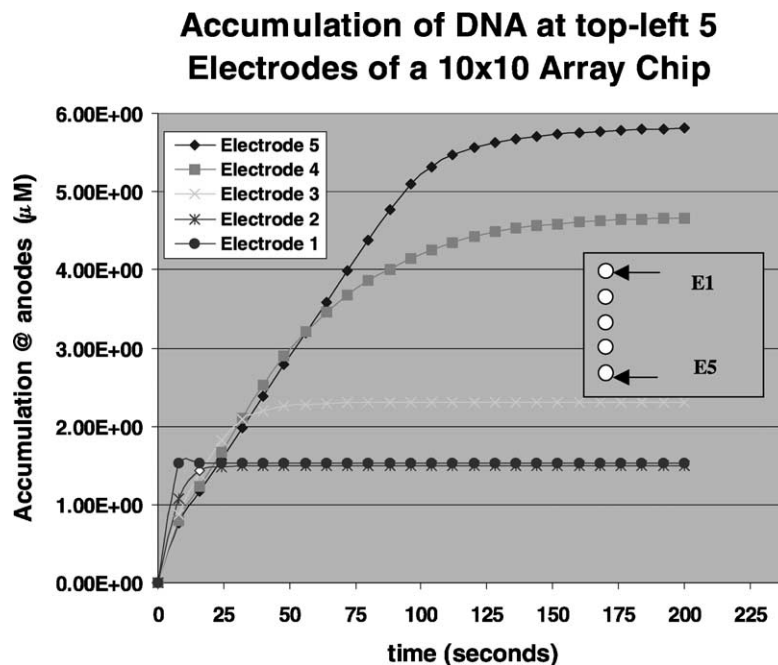


Fig. 14. Accumulation of DNA at the electrodes of a 100-site chip with respect to time.

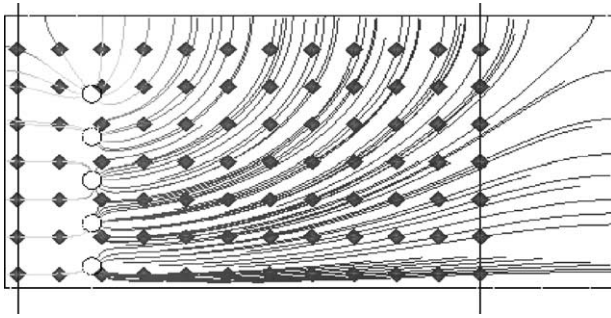


Fig. 15. Streak lines of electric field in a symmetrical-half of a 100-site chip depicting path that will be followed by DNA species as they move towards the anodes.

of DNA as shown in the figure. The middle electrode located at the bottom starts with the minimum accumulation in the first few seconds; but nevertheless manages to accumulate the most at the end of the simulation run (i.e. 200 s). The implication of this observation is that for a solution containing a small concentration of species, most of the accumulation in the first few seconds will be at the outer-edge electrodes.

3.4. Experimental results

Numerous experiments were run on the 400-site chip to validate the model predictions previously described. The on-chip electronics in the 400-site chip permit independent control of the potential at each array electrode and independent measurement of the current at each electrode. In the experiments described below the potential on the array electrodes was held constant with respect to the QRE. Current measurements were directly taken from each array electrode.

In the first set of experiments, the fluid chamber containing the chip was filled with 5 mM histidine buffer. The array electrodes on column 1 were biased at +2 V while both the long and short counter-electrodes were biased at -2 V. The resulting currents simultaneously measured at each array electrode are shown in Fig. 16. The qualitative pattern of current distribution is similar to the pattern predicted by sim-

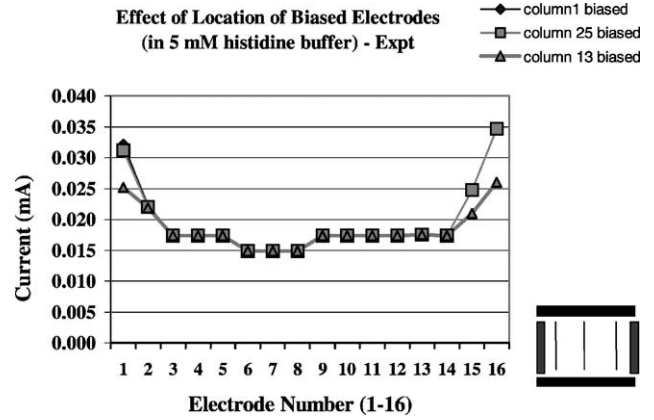


Fig. 16. Current distribution in a 400-site chip showing effect of location of biased electrodes.

ulation for the electric field distribution previously shown in Fig. 10 wherein geometric effects at the outer-edge electrodes are prominent. Note that there is a direct correlation between electric field strength and current. Further, a qualitatively similar pattern is observed when columns 13 (middle) and 25 (right outer-edge array electrodes) are positively biased. Further, Fig. 16 compares the variation in current distribution as the location of biased electrodes is moved from the edges to the center.

In the next set of experiments, we investigated the effect of the short (vertical) and long (longitudinal) counter-electrodes on electric field and current distribution. The solution used was de-ionized (DI) water which was observed to exhibit peaking effects when all pads were turned on. First, the long counter-electrodes were biased along with the electrodes on the first set of columns. As shown in Fig. 17, the geometric effects still existed, even though the magnitude of the peaks had slightly decreased. In the second experiment, only the short pads were biased negatively. Again, as shown in Fig. 17, the peaking effects, in this case, were significantly diminished. In summary, as predicted by the FEA simulation, when a column of electrodes is biased, the long counter-electrodes have a stronger effect than the

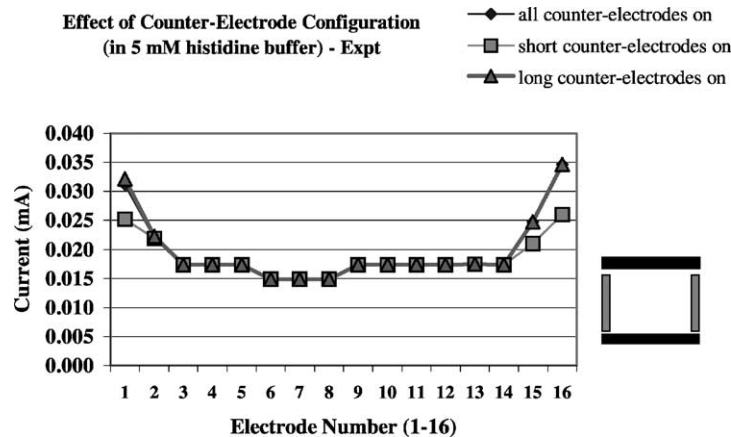


Fig. 17. Effect of counter-electrode configuration on current density distribution in a 400-site chip.

Table 2
Buffers used in experiments on the 400-site chip

Buffer type	Conductivity ($\mu\text{S}/\text{cm}$)
DI water	— ^a
0.5 mM histidine	1.0
1.0 mM histidine	1.0
2.5 mM histidine	3.0
5.0 mM histidine	7.0
12.5 mM histidine	14.0
25.0 mM histidine	31.0
50 mM histidine	58.0
0.001 mM NaNO_3	330.0

^a For simulation purposes, a conductivity of $0.6 \mu\text{S}/\text{cm}$ was used.

short counter-electrodes on the current peaking at the outer electrodes. Also, as predicted by the FEA simulation, the peaking observed when all counter-electrodes are biased is due mostly to the long counter-electrodes.

In the last set of experiments, we investigated the effect of conductivity of the buffer solution on current distribution. The buffers used along with their measured conductivities are given in Table 2.

As shown in Fig. 18, the current distributions tend to be uniform as the conductivity of the solution increases. For histidine, concentrations of 0.5, 1.0, 2.5, and 5.0 mM show the peaking effect, whereas concentrations above and including 12.5 mM do not show the peaking of electric field and currents at the outer-edge electrodes. For NaNO_3 , a non-zwitterionic electrolyte, the geometric effect of peaking electric fields at the outer-edge electrodes was eliminated at concentrations as low as 0.001 mM. Generally, above approximately 12.5 mM concentration of histidine, the current distributions are flat. We believe that the flattening of the current distributions is a consequence of the polarization resistance (which is not affected by geometrical arrangement of the electrodes) being the dominant resistance when the solution conductivity is high. This topic is discussed further below.

3.4.1. AC impedance studies

AC impedance study was performed on the 100-site chip array (cf. Fig. 1a) to further corroborate the geomet-

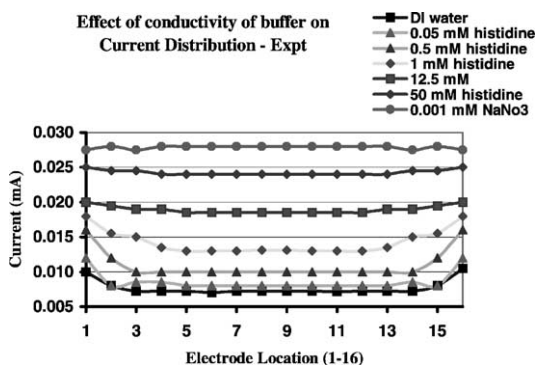


Fig. 18. Effect of conductivity of buffer solution on electric field distribution in 400-site chip.

ric effect of peaking of electric field and currents at the outer-edge electrodes. No permeation layer was used. Autolab Eco Chemie potentiostat/frequency response analyzer, Model PGSTAT20 was used to apply a sinusoidal AC signal (10 mV amplitude, frequency range 20–5 Hz) between the array electrodes. The DC potential (E_{DC}) was controlled with respect to Ag/AgO QRE surrounding the electrode array. Contact to individual electrodes allowed measurement of geometric effects, i.e. effect of location of the electrodes on the impedance signal.

Fig. 19 shows impedance spectra obtained at $E_{\text{DC}} = 0.0 \text{ V}$ between two array electrodes (1.1 and 1.10; first number designates row and second number designates column) as a function of histidine concentration. The spectra exhibit typical Randles equivalent circuit circular shape (cf. Fig. 20). By increasing the concentration of histidine the semicircles become smaller, indicating higher current due to higher concentration of the electroactive species in solution. At zero potential applied, the Faradaic reactions are minimal and the current and/or polarization resistance is determined by the concentration of impurities which are the source of the electroactive species. At increased electrolyte concentrations, Faradaic currents increases and the polarization resistance decreases. This is evident as a decrease in the semicircle diameter in Fig. 19. In this case, the solution resistance is relatively small compared to polarization resistance because the distance between the electrodes in the array is small and no dominant electroactive species such as a redox pair is present in solution. However, solution resistance changed with increased concentration.

When the potential is moved into a region of oxygen evolution, contribution of the Faradaic currents to total current increases compared to the case where $E_{\text{DC}} = 0.0 \text{ V}$. Fig. 21 shows impedance diagrams obtained at $E_{\text{DC}} = 1.3 \text{ V}$ where oxygen evolution reaction takes place. The spectra became smaller with increased concentration of the electrolyte. Also, comparing the spectra obtained in Fig. 19 (at $E_{\text{DC}} = 0.0 \text{ V}$) with the spectra obtained at $E_{\text{DC}} = 1.3 \text{ V}$, the polarization resistance decreased in the latter case. Polarization resistance, R_p , and solution resistance, R_s , were calculated for all impedance spectra using a least-square method fit for a semicircle as shown in Fig. 20. Table 3 shows values for R_p/R_s ratios for different concentrations and at the two potentials measured. At low conductivity, i.e. DI water and at low electrolyte concentrations, the R_p/R_s ratio at $E_{\text{DC}} = 0.0 \text{ V}$ is up to two orders of magnitude higher compared to

Table 3
Variation of the ratio of polarization resistance to solution resistance for different buffers

Buffer type	R_p/R_s	
	0.0 V	1.3 V
DI water	30000	1000
12.5 mM histidine	1000	500
50.0 mM histidine	300	100

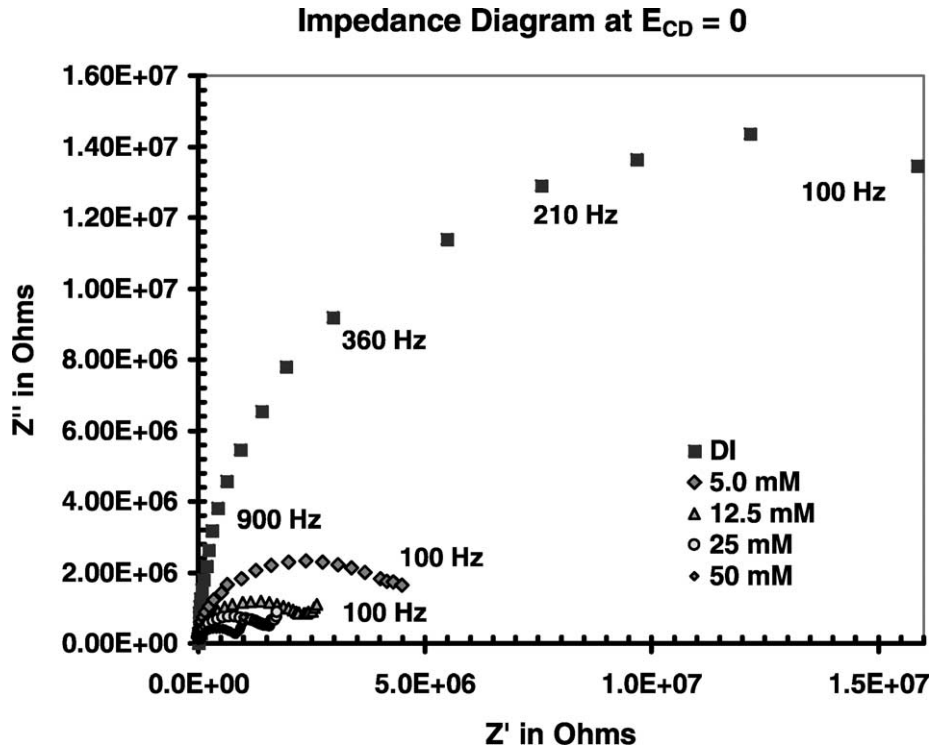


Fig. 19. Impedance diagram for buffers of different concentrations at $E_{DC} = 0.0$ V.

higher electrolyte concentrations. This trend is also observable at $E_{DC} = 1.3$ V, although the decrease in the R_p/R_s ratio with concentration is smaller, i.e. up to 10-fold decrease. The results shown in Table 3 clearly demonstrate that

at low electrolyte concentrations the total resistance is very high, and is dominated by the polarization resistance. Consequently, the total currents at the electrode array are very small and solution resistance is affected by the geometrical

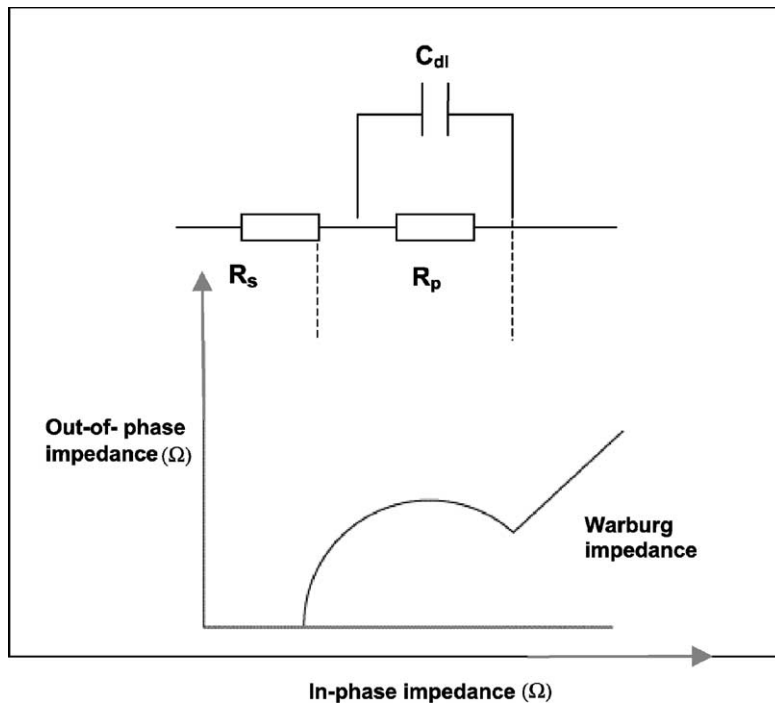


Fig. 20. Equivalent circuit diagram for impedance test.

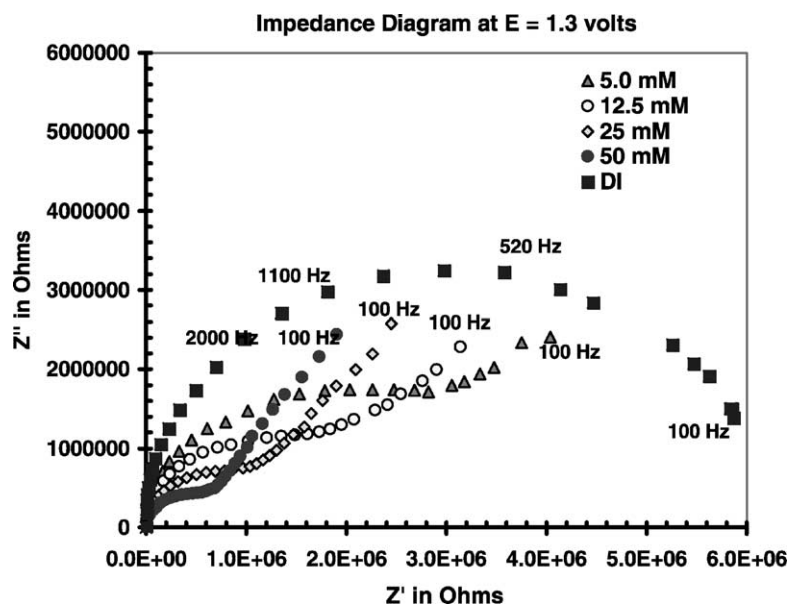


Fig. 21. Impedance diagram for buffers of different concentrations at $E_{DC} = 1.3$ V.

arrangement of the electrodes. If the electrolyte concentration is increased, the polarization resistance decreases and allows much higher Faradaic currents. Total current is dominated by the polarization resistance which screens the effects of solution resistance, thus the geometrical effects become negligible. This explanation supports the observation of the disappearance of current peaks at the edge electrodes at higher electrolyte concentrations (cf. Figs. 9–11 and 13). In our DNA chip applications, we utilize 50 mM histidine as a low-salt buffer to promote the electrophoretic transport of DNA. At this electrolyte concentration, as shown above, geometric effects are negligible, i.e. current peaks at edge electrodes are not observed. This assures uniform electric field distribution throughout the electrode array and uniform accessibility of the target or probe molecules to all electrodes.

Impedance data in Figs. 19 and 21 also exhibit a linear portion of the impedance spectra at lower frequencies. The phase angle of the linear portion approaches 45° which indicates a diffusion controlled process in accordance to Warburg impedance. The Warburg impedance seems to be observable both at $E_{DC} = 0.0$ and 1.3 V indicating diffusion of electro-active impurities and oxygen species, respectively. A more thorough AC impedance investigation could provide insight into protonation of histidine and further understanding of diffusion processes in low-salt buffer electrolytes containing amino acids. These studies are in progress.

4. Discussion

Table 1 showed a comparison of two models and experimental data indicating that the amount of accumulated DNA in 60 s was approximately 1–2% of the total amount ap-

plied to the chip. The conditions of this experiment were that only one array electrode was biased at a constant current of 400 nA for one minute. Although the total amount of DNA accumulated is small compared to the volume applied, the 1–2% accumulation on an electrode of $80 \mu\text{m}$ represents a concentration increase over the array electrode of two to three orders of magnitude. For example, in the volume $2 \mu\text{m}$ above the array electrode, the concentration increases from 5 nM to $2.5 \mu\text{M}$, a 1500-fold increase in concentration. This significant increase of concentration at the electrodes generates counter-diffusion and repulsion due to similar valency that resist further accumulation of DNA. For higher concentration of DNA commonly used in these chips, this magnitude of accumulation at a single electrode is found to be quite adequate. Further, at lower concentrations of the analyte, lower and controlled accumulation of DNA per pad may be desirable to achieve uniform analyte distribution when multiple electrode addressing is performed.

Attempts have been made to increase the accumulation by using a series of focusing electrodes [12,20]. Under conditions of extremely low target concentrations, this might have some benefit. However, without the use of focusing electrodes we have been able to reproducibly detect labeled, synthetic targets with as few as 10^6 molecules. At higher concentrations typical of the amplicon concentrations from PCR or SDA amplification reactions, the targets tend to saturate the array electrodes during addressing. This can be seen in Fig. 8 where the accumulation starts to plateau after approximately 80 s. Furthermore, the concentration of accumulated target exceeds the binding capacity of the permeation layer covering the electrodes. Because the target concentrations from PCR and SDA reactions are very high, we find the use of focusing electrodes unnecessary in most practical applications.

The FEA simulations showed that the geometry of array of biased electrodes has a significant bearing on the electric field strengths at the array electrode locations. This was corroborated by experiments in low conductivity buffers on the 400-site chip. In low conductivity solutions, the solution resistance is high and represents the predominant resistance in the circuit. Because of the close proximity of the outer array electrodes to the counter-electrodes the solution resistance is lower compared to the inner array electrodes. Furthermore, the outer array electrodes tend to screen the long counter-electrodes such that the inner array electrodes experience a diminished field. Alternatively, this could also be seen as a case where the electric field lines of interior electrodes are screened by the electric field lines of their neighboring electrodes on both sides, whereas the electric field lines of the outer electrodes are affected only in the interior side. The combination of these effects results in the electric field distribution and current distribution shown in Figs. 10a and b, 12a–d and 16, respectively.

In buffers with conductivities approximately above 12.5 mM histidine, the experimental results show little or no effect of the geometry of biased electrodes on the current and electric field distribution, and they are practically uniform. In buffers with higher conductivity, polarization resistance decreases significantly, i.e. Faradaic currents dominate the overall resistance. Thus, the geometric effects on the solution resistance and the overall current distribution at the electrode array are not observed. Because FEA simulations do not account for polarization resistance, they are unable to predict the Faradaic currents and hence the uniform field distribution above 12.5 mM histidine. Earlier studies reported in the literature where FEA was used [13], therefore, will fail in accurately predicting electric field distribution for buffers of higher conductivity.

In diagnostic assays, we typically use 50 mM histidine or similar electrolytes as the transport buffer. At 50 mM concentration of histidine, the charge transfer resistance dominates the circuit resistance. Consequently, the accumulation should be uniform across all the array electrodes. Fig. 8 shows that within experimental error, the accumulation is uniform.

5. Conclusions

This study demonstrates the simulation of the transport and accumulation phenomenon in an active DNA biochip array. Important quantities such as radial and depth-wise electric field distribution, DNA species transport and accumulation are modeled and their results compared with experimental findings and a simplified analytical model. The simulations indicated that understanding the electric field distribution, the driving force for electrophoretic DNA transport is crucial for the cell design and optimizing DNA accumulation at the electrodes. The finite element analysis modeling included the effect of diffusion which cannot be

ignored if close correlation with experimental results is intended. Both experimental and modeling results confirmed that electronic addressing of DNA at the electrodes offers substantial advantages compared to passive transport controlled solely by diffusion. DNA accumulation is achieved within seconds at a locus of fluorescence detection. The modeling results were in close correlation with the experimental results, providing a design tool for optimizing the conditions for accumulation of DNA with respect to electric field applied, time of accumulation, targeted detection sensitivity, and the number of electrodes or detection loci.

Further, the following observations were made:

1. In chips with array of electrodes and buffers of low conductivity, geometry effects introduce a current distribution that has peaks on outer-edge electrodes.
2. For buffers with increased conductivity such as histidine (12.5 mM and above) and NaNO₃ (0.001 mM and above), the geometric effects are significantly reduced.
3. Experimental results indicate that the location of the biased electrodes also affects the current distribution and the magnitude of the peaks. Electric pads in the geometric center seem to experience less peak as compared to the edge electrodes.
4. The decrease in these geometric effects is caused by the charge transfer mechanism between electrodes and the buffer (i.e. Faradaic current). Numerical models that do not explicitly include the charge transfer mechanism in their formulation will fail in predicting the decrease and elimination of these effects with increased buffer conductivity.
5. From a consideration of electric field strength, flow cell depths could be kept as small as possible without reducing the electric field strength. However, due to fluidics considerations, oxygen saturation and bubble formation in the chip, the depth of the cell has to be significantly higher.

References

- [1] P. Deloukas, et al., A physical map of 30,000 human genes, *Science* 282 (1998) 744–746.
- [2] R. Radtkey, L. Feng, M. Muralhider, D. Canter, D. DiPierro, S. Fallon, E. Tu, K. McElfresh, M. Nerenberg, R. Sosnowski, Rapid high fidelity analysis of simple sequence repeats on an electronically active DNA microchip, *Nucl. Acids Res.* 28 (7) (2000) E17.
- [3] R. Sosnowski, E. Tu, W. Butler, J. O'Connell, M. Heller, Rapid determination of single base mismatch mutations in DNA hybrids by direct electric field control, *Proc. Natl. Acad. Sci.* 94 (1997) 1119–1123.
- [4] P. Gilles, D. Wu, C. Foster, P. Dillon, S. Chanock, Single nucleotide polymorphic discrimination by an electronic dot blot assay on semiconductor, *Nat. Biotechnol.* 17 (1999) 365–370.
- [5] M. Chee, R. Yang, E. Hubbell, A. Berno, X. Huang, D. Stern, J. Winkler, D. Lockhart, M. Morris, S. Fodor, Accessing genetic information with high-density DNA arrays, *Science* 274 (1996) 610–614.

- [6] T. Taton, C. Mirkin, R. Letsinger, Scanometric DNA array detection with nanoparticle probe, *Science* 289 (2000) 1757–1760.
- [7] R. Umek, S. Lin, J. Vielmetter, R. Terbrueggen, B. Ivine, C. Yu, J. Kayyem, H. Yowanto, G. Blackburn, D. Farkas, Y. Chen, Electronic detection of nucleic acids: a versatile platform for molecular diagnostics, *J. Mol. Diagnost.* 3 (2) (2001) 74–84.
- [8] C. Edman, D. Raymond, D. Wu, E. Tu, R. Sosnowski, W. Butler, M. Nerenberg, M. Heller, Electric field directed nucleic acid hybridization on microchips, *Nucl. Acids Res.* 25 (24) (1997) 4907–4914.
- [9] C.F. Edman, R.B. Swint, C. Gurtner, R.E. Formosa, S.D. Roh, K.E. Lee, P.D. Swanson, D. Ackley, J.J. Coleman, M.J. Heller, Electric field directed assembly of an InGaAs LED onto silicon circuitry, *IEEE* 12 (9) (2000) 1198–1200.
- [10] E. Tu, A.H. Forster, M.J. Heller, Active microelectronic chip devices which utilize controlled electrophoretic fields for multiplex DNA hybridization and other genomic applications, *Electrophoresis* 21 (2000) 157–164.
- [11] J. Cheng, E.L. Sheldon, L. Wu, A. Uribe, L.O. Gerrue, J. Carrino, M.J. Heller, J. O’Connell, Electric field controlled preparation and hybridization analysis of DNA/RNA from *E. coli* on microfabricated bioelectronic chips, *Nat. Biotechnol.* 16 (1998) 541–546.
- [12] M. Stelzle, M. Durr, W. Nisch, On-chip electrophoretic accumulation of DNA-oligomers and streptavidin, *Fresenius J. Anal. Chem.* 371 (2001) 112–119.
- [13] M. Paces, J. Lindner, J. Havlica, J. Kosek, D. Snita, M. Marek, Mathematical modeling of complex chemical microsystems in electric field, in: *Proceedings of the Fourth International Conference on Microreaction Technology (IMRET 4)*, Atlanta, 5–9 March 2000.
- [14] M. Ozkan, Development of opto-electrokinetic addressing tools for the assembly of biological cells and optoelectronic devices in microarrays, PhD Dissertation, Department of Electrical Engineering, University of California, San Diego, CA, 2001.
- [15] Covantor Inc., *CovantorWare™ Reference Guide*, Cary, NC, 2002.
- [16] L. Wu, DNA transportation—simple analytical approach, Personal communication, 1996.
- [17] J. Newman, Resistance for flow of current to a disk, *J. Electrochem. Soc.* 113 (1966) 501–502.
- [18] R. Ferrigno, P.F. Brevet, H.H. Girault, Finite element simulation of the chronoamperometric response of recessed and protruding microdisc electrodes, *Electrochim. Acta* 42 (12) (1997) 1895–1903.
- [19] Corning-IntelliSense Inc., *User’s Manual*, Wilmington, MA, 2002.
- [20] D. Ackley, P. Swanson, S. Graham, E. Mather, T. Leclair, W. Butler, Advanced active electronic devices for molecular biological analysis and diagnostics, Patent 6,099,803, USPTO, 8 August 2000.

Biographies

Samuel K. Kassegne received his PhD degree in engineering mechanics from Virginia Tech in 1992. He had also received his undergraduate degree in civil engineering from Anna University in India in 1984 and MS degree in structures from the Middle East Technical University, Ankara, Turkey in 1987. He has extensive experience in design and characterization of mechanical and electrical miniaturized devices including MEMS and BioMEMS. His current interests include characterization and simulation of the electrokinetic transport and hybridization of biomolecules in porous membrane structures in micro-arrays. He is currently a principal engineer at Nanogen Inc., which he joined in 2001. He also teaches part time finite element analysis and MEMS courses at the University of California at San Diego extension.

Howard Reese obtained his PhD in chemistry from the University of California, San Diego in 1989 where he studied the physics of DNA in extensional flow fields. Following his graduate work, he received an NIH postdoctoral fellowship to investigate the mechanisms of DNA electrophoresis. While working on his fellowship, he also hosted the

Science and Technology public science seminars at the University of Oregon. Currently, he is employed at Nanogen Inc. where he continues to work on DNA micro-array technology.

Dalibor Hodko obtained his PhD and MSc degrees from the University of Zagreb, Zagreb, Croatia in 1990 and 1984, respectively. He also has a BSc degree from University of Zagreb in chemical engineering. Currently, he is the director of Advanced Technology Group at Nanogen Inc. He is a recognized physical chemist with broad experience in developing miniaturized analytical instrumentation. He has served as a principal investigator on more than 25 federally funded projects and has broad experience in conducting and performing R&D received through peer reviewed government support.

Joon M. Yang received his BS, MS, and PhD degrees from the Department of Mechanical Engineering of Seoul National University (Korea) in 1989, 1991, and 1996, respectively. After completing his PhD degree, he was a postdoctoral fellow of the Mechanical and Aerospace Engineering Department of University of California at Los Angeles (UCLA) from 1996 to 1999. He is currently a staff scientist/engineer at Nanogen Inc. His research interests include microfluidics, microfluidic devices, BioMEMS devices, and their package/instrumentation.

Kamal Sarkar received his undergraduate degree in mechanical engineering from Calcutta University in India. He specialized in material science from IIT, Kanpur, and received his PhD in materials engineering from the University of Tennessee, Knoxville, in 1980. He has more than 20 years of product development and process improvement experience in a variety of industries, including, medical device, biotechnology, materials, and recreational. His recent interests include MEMS and NEMS devices, nanofibers, single molecule detection, and simulation of charged species under pressure driven and EK (electro-kinetic) flows. He has three patents and numerous research reports including “the most outstanding” paper of the 1995 Society of Plastics Engineers, Medical Plastics Division.

Dan Smolko received his BS degree in chemical engineering from the University of Kentucky followed by a PhD degree in chemical engineering and a Minor in biotechnology from North Carolina State University in 1994. He has extensive experience in biosystems R&D, systems integration, microreaction molding, genetic engineering, and bacterial and cell culture methodologies. He is currently a senior research scientist in the Advanced Technology Group at Nanogen Inc.

Paul Swanson received his BS, MS, and PhD in electrical engineering from the University of Illinois in 1983, 1985, and 1989, respectively. After his PhD, he was a postdoctoral associate at Cornell University and a research associate at the Rome Laboratory Photonics Center. Currently he is a principal engineer at Nanogen Inc. He has been responsible for the design and in-house fabrication of almost every Nanogen micro-electrode array chip. His professional interests include system design, MEMS device fabrication, and the underlying physical processes of MEMS devices.

Daniel E. Raymond obtained BSc in chemistry in 1985 from the University of Victoria, BC, Canada, and in 1993 obtained a PhD in analytical chemistry from the University of Alberta, Alberta, Canada. He is currently a principal scientist at Genoptix Inc., in San Diego, CA. His research interests involved electrochemical applications toward DNA diagnostics and microfluidic applications for cell-based assays.

Michael J. Heller received his PhD in biochemistry from Colorado State University. His rich scientific experience includes working as NIH postdoctoral fellow at Northwestern University, supervising the DNA Technology Group at Amoco Corporation, and serving as the director of Molecular Biology at Molecular Biosystems Inc. In 1987 he was elected president and chief operating officer at Integrated DNA Technologies. He was also a co-founder and the chief technical officer at Nanogen Inc., and the

principal inventor of Nanogen's microelectronic-based DNA chip technology. He presently serves as a consultant to Nanogen Inc. His experience includes many areas of biotechnology, with particular expertise in DNA molecular diagnostics and fluorescent/optoelectronic-based detection technologies. His most recent work involved the development of integrated DNA chip devices and systems for genomic and biomedical research and clinical diagnostic applications. He has also been involved in the development of biosensor systems for the detection of infectious agents related to national response to bioterrorism. He served on the White House National Nanotechnology Initiative Panel in 1999/2000, and is presently serving on the NAS National Nanotechnology Initiative Review Panel.

Marc J. Madou received his PhD (summa cum laude) in semiconductor electrochemistry, at the Solid-State Physics Laboratory, Rijksuniversiteit, Ghent, Belgium. He also received his BSc, MSc from the

same university in physical chemistry in 1973 and 1975, respectively. He is currently a professor of Mechanical and Aerospace Engineering at UC Irvine and also a NASA Ames Research Center associate. He has conducted sensor research with industrial applications such as automotive sensors as well as for environmental. His mechanical sensor research includes AFM tips, pressure sensors and accelerometers. In basic research, he is interested in applying micromachining to explore new physics and chemistry by working with micromachined devices where macro physical laws break down. He has also worked at Nanogen Inc., as the vice president of Advanced Technology from 2001 to 2002. He is the editor for North and South America for *Sensors and Actuators B* and organizer of the annual San Francisco BioMEMS Conference. He has also written two books in the area of MEMS and BioMEMS and is internationally known both academically and industrially as an expert in this field.